Electric transport across $Sr_{1-x}La_xCuO_2$/Au/Nb planar tunnel junctions and x-ray photoelectron and Auger-electron spectroscopy on $Sr_{1-x}La_xCuO_2$ thin films

J. Tomaschko,[1] C. Raisch,[2] V. Leca,[1,3] T. Chassé,[2] R. Kleiner,[1] and D. Koelle[1,*]

[1]*Physikalisches Institut–Experimentalphysik II and Center for Collective Quantum Phenomena in LISA$^+$, Universität Tübingen, Auf der Morgenstelle 14, 72076 Tübingen, Germany*

[2]*Physikalische Chemie and LISA$^+$, Universität Tübingen, Auf der Morgenstelle 18, 72076 Tübingen, Germany*

[3]*Faculty of Applied Chemistry and Materials Science, University Politehnica of Bucharest, Gheorghe Polizu Street 1-7, Bucharest 011061, Romania*

(Received 10 March 2011; revised manuscript received 8 June 2011; published 24 August 2011)

Thin-film planar tunnel junctions with the electron-doped infinite-layer superconductor $Sr_{1-x}La_xCuO_2$ (SLCO) with $x \sim 0.15$ as bottom electrode, a thin Au interlayer, and Nb as top electrode were fabricated and characterized. Measurements of electric transport across these junctions provide information on the interface and surface properties of the SLCO thin films. No Cooper pair tunneling is observed; however, nonlinear current-voltage characteristics give evidence for quasiparticle (QP) tunneling across a thin insulating SLCO barrier at the SLCO/Au interface, with a single gap value ∼1.4 meV, originating from superconducting Nb. The absence of a superconducting SLCO gap in the QP conductance curves indicates a thin normal-conducting SLCO layer below the insulating SLCO barrier. To examine its origin, x-ray photoelectron spectroscopy (XPS) and x-ray Auger-electron spectroscopy (XAES) on SLCO thin films were performed. We observe a Cu valence of +1 in the SLCO surface layer (within ∼3 nm thickness) and of +2 in deeper regions, as expected for fully oxidized CuO_2 planes in the bulk. Hence, the XPS and XAES results for the SLCO films are consistent with the QP tunneling spectra observed for our planar SLCO/Au/Nb junctions.

DOI: 10.1103/PhysRevB.84.064521 PACS number(s): 74.72.Ek, 74.50.+r, 74.78.Fk, 82.80.Pv

I. INTRODUCTION

Both, hole- and electron-doped high-transition-temperature (T_c) cuprate superconductors have been synthesized and investigated intensively throughout the past two decades. On the electron-doped side only two families of cuprate compounds are known. These are the T' compounds[1,2] $L_{2-x}Ce_xCuO_4$ ($L =$ La,Pr,Nd,Sm,Eu) with maximum $T_c =$ 30 K and the infinite-layer (IL) compounds[3,4] $Sr_{1-x}L_xCuO_2$ ($L =$ La,Pr,Nd,Sm,Gd) with maximum $T_c = 43$ K. The IL crystal structure is formed by alternating stacks of CuO_2 and $Sr_{1-x}(L_x)$ (a-b) planes along the c-axis direction. The charge reservoir block, commonly present in cuprate superconductors, as well as apical oxygen do not exist in the ideal IL crystal lattice.[5] Electron doping is suggested because the nominal Sr and L valences are +2 and +3, respectively.[4] As the crystal structure of the IL compounds is the simplest of all cuprate superconductors, they provide a unique opportunity to explore the fundamental nature of high-T_c superconductivity. For the same reason, they are often referred to as the "parental structure" of cuprate superconductors.[6] However, due to severe difficulties in the synthesis of high-quality samples, the IL cuprates have been much less examined than any other cuprate superconductors. In particular, no large single crystals of the IL compounds have been synthesized so far, and the synthesis of polycrystalline bulk material requires high pressure (≈1 GPa).[7–9] To overcome this problem, epitaxially grown, single-crystal IL thin films have been fabricated, where the pressure is supplied by epitaxial strain.[10,11] Karimoto *et al.*[12] succeeded in synthesizing electron-doped IL thin films with T_c close to the bulk value by molecular beam epitaxy (MBE) on $KTaO_3$ (KTO) substrates, supplying tensile strain, which is believed to support the electron-doping effect for the CuO_2 planes. Moreover, they confirmed that, under the oxidizing conditions generally used during deposition, vacuum annealing of the as-grown film is essential for superconductivity to emerge. Without this reduction step, excess oxygen occupies interstitial sites in the Sr(L) planes and localizes electrons, which in turn hampers superconductivity. This reduction step was established in T' compounds before[13] and is nowadays a common synthesis step for IL thin films grown by various techniques, such as sputtering,[11,14] pulsed laser deposition (PLD)[15,16] and MBE.[12,17] Yet, too strong reduction ends up in the formation of ordered oxygen vacancies in the CuO_2 planes. This phase is called the "long-c-axis" phase or the "infinite-layer-related" (IL-r) phase,[15,18] which suppresses superconductivity.[12,14] The unit cell of the IL-r phase is a superstructure of the IL unit cell with lattice parameters $2\sqrt{2}a_p \times 2\sqrt{2}a_p \times c_s$, where a_p is the in-plane parameter of the perovskite-type IL structure with tetragonal symmetry and c_s is the superstructure-extended c-axis parameter with $c_s \approx 3.6$ Å (compared to $c \approx 3.4$ Å for the IL structure).

To examine the influence of vacuum annealing on the surface of our PLD-grown $Sr_{1-x}La_xCuO_2$ (SLCO) thin films, we performed surface-sensitive electric transport measurements, x-ray photoelectron spectroscopy (XPS) and x-ray Auger-electron spectroscopy (XAES). Our transport measurements were carried out on planar SLCO/Au/Nb tunnel junctions. Quasiparticle tunneling was observed, which we attribute to an insulating barrier at the SLCO/Au interface and a thin normal-conducting SLCO layer below this barrier. To identify its origin, XPS studies on SLCO thin films were performed, revealing a reduced Cu species with valence +1 in the surface layer (∼3 nm thick) of SLCO. This result is consistent with the findings of other groups[19–21] who performed corresponding studies on CuO and Cu_2O samples.

Moreover, to our knowledge, we performed the first XPS and XAES studies on the (insulating) IL-r phase, allowing us to pinpoint the spectral lines of the superconducting IL phase by comparing the spectra with each other. Furthermore, x-ray diffraction studies indicate the presence of an approximately 3-nm-thick disordered SLCO surface layer, supporting our planar tunneling, XPS, and XAES results.

II. SAMPLE FABRICATION AND EXPERIMENTAL DETAILS

A polycrystalline $Sr_{1-x}La_xCuO_2$ ($x = 0.125$) target[22] was used for epitaxial growth of 25- to 30-nm-thick SLCO films on (001) KTO substrates[23] at 580 °C and 20 Pa oxygen pressure, by pulsed laser deposition, using a KrF ($\lambda = 248$ nm) excimer laser with a repetition rate of 2 Hz. The base pressure of the PLD chamber was 10^{-6} Pa. *In situ* high-pressure reflection high-energy electron diffraction (RHEED) was used to monitor the growth mode and growth rate by counting the number of deposited monolayers within the first 5 to 30 unit cells. In order to remove excess oxygen from the Sr/La planes, after thin-film deposition the samples were annealed in vacuum (10^{-5} Pa) at 580 °C for 5–10 min before cooling down to room temperature.

For the fabrication of planar tunnel junctions, the samples were transferred in vacuum ("*in situ*") to an electron beam evaporation chamber, where a 5-nm-thick Au layer was evaporated on top of SLCO. The Au thickness was sufficient to cover all asperities of the underlying SLCO layer; atomic force microscopy in contact mode on SLCO thin-film reference samples revealed a root mean square roughness of 0.3 to 0.7 nm. Subsequently, the samples were transferred *in situ* to a magnetron sputtering chamber where a 21-nm-thick Nb film was sputtered on top of the Au layer. The SLCO/Au/Nb trilayers were removed from the deposition system and patterned to form planar SLCO/Au/Nb junctions with lateral dimensions of $5 \times 30\ \mu m^2$ by standard photolithography and Ar ion milling. This involved sputtering of an additional 5-nm-thick Au layer and subsequently a 100-nm-thick Nb layer, which was etched down to 75 nm thickness later on during the patterning process (see Fig. 1). For a detailed description of the fabrication process see Ref. 24. Altogether, we fabricated two chips, each of which had five SLCO/Au/Nb junctions with nominally identical geometry. Electric transport properties were measured in the temperature range $T = (4.2–300)$ K in a magnetically and radio frequency shielded setup using feed lines with high-frequency-noise filters.

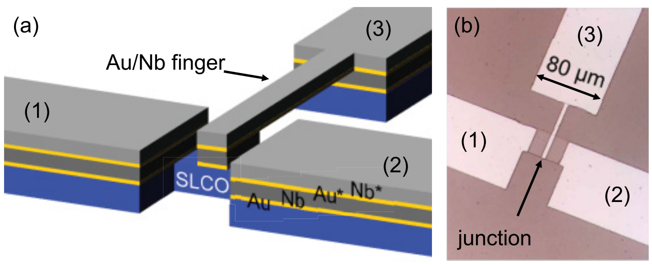

FIG. 1. (Color online) Schematic layout (a) and micrograph (b) of planar SLCO/Au/Nb junction. The stacking sequence from bottom to top is SLCO (26 nm)/Au (5 nm)/Nb (21 nm)/Au* (5 nm)/Nb* (75 nm). The first three layers forming the junction were deposited *in situ*. The uppermost two layers (labeled with *) are required for the patterning process (Ref. 24).

In order to obtain element-specific information regarding the chemical state (valence) of SLCO, XPS and XAES were performed. For these studies, two SLCO thin films—SLCO-1 and SLCO-2—were grown under the same conditions, with the same thickness, as described above and transferred to the XPS/XAES setup immediately after growth to minimize surface contamination. The system (base pressure 5×10^{-8} Pa) consists of a SPECS XR 50 Mg $K\alpha$ x-ray source and a SPECS Phoibos 100 hemispherical energy analyzer. The pass energy was set to 20 eV for all experiments, yielding an energy resolution of ≈ 1 eV. By tilting the sample about an angle θ, the information depth could be further reduced by a factor of $\cos\theta$. In our experiments the samples were measured at $\theta = 0°$ (normal incidence) and $\theta = 60°$ (grazing incidence), corresponding to an information depth of ≈ 6 and ≈ 3 nm, respectively. The samples could be heated in the XPS/XAES setup to examine the effect of vacuum annealing. After initial XPS analysis, sample SLCO-1 was annealed at low temperature ($T \approx 350$ °C, $t = 30$ min) and sample SLCO-2 at high temperature ($T \approx 550$ °C, $t = 5$ min) and then measured again. For data obtained after annealing in the XPS/XAES setup we refer to these samples as SLCO-1a and SLCO-2a. After XPS analysis, the crystal structures of the SLCO thin films were characterized by x-ray diffraction (XRD) using a Panalytical X'Pert system equipped with a Cu cathode and monochromator.

III. ELECTRIC TRANSPORT PROPERTIES

In this section we present and discuss results obtained on the electric transport properties of one of the planar SLCO/Au/Nb junctions. A second junction on the same chip and two other junctions on the second chip showed very similar behavior.

A. Technical aspects

For electric transport measurements, the sample was contacted in a two-point arrangement, with bias current I flowing from pad 1 along the SLCO layer, through the SLCO/Au/Nb junction and the Au/Nb finger to pad 3 (see Fig. 1); the voltage V was detected across the same two pads. For T below the Nb transition temperature $T_{c,\mathrm{Nb}}$, the Au layers are expected to become superconducting due to the proximity effect. In this case, we have a four-point arrangement. Electrodes 1 and 2 were used for characterization of the 39-μm-long and 30-μm-wide bottom SLCO layer (see Fig. 1).

To sort out parasitic signals from the upper Au layer, we checked the above-mentioned proximity effect by fabricating a reference Nb/Au/Nb junction, which had the same geometry as the SLCO/Au/Nb junction. The fabrication process for this reference sample was nominally identical to the process for the upper Nb-Au-Nb layers in the SLCO/Au/Nb/Au/Nb samples, i.e., the Au layer and the upper Nb layer were deposited after exposing the bottom Nb layer to *ex situ* conditions. Below $T_{c,\mathrm{Nb}}$, the reference sample showed no voltage drop up to the critical current $I_{c,\mathrm{Nb}}$ of the Au/Nb finger. Thus, for $T < T_{c,\mathrm{Nb}}$ and $I < I_{c,\mathrm{Nb}}$, any voltage signal detected

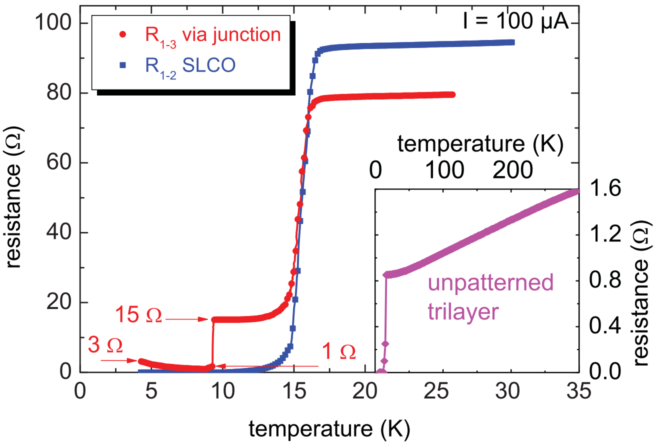

FIG. 2. (Color online) Resistance R vs temperature T measured across the SLCO/Au/Nb junction ($R_{1\text{-}3}$) and along the SLCO bottom layer ($R_{1\text{-}2}$). Inset: $R(T)$ of the unpatterned SLCO/Au/Nb trilayer.

for the SLCO/Au/Nb/Au/Nb samples must stem from the SLCO/Au/Nb junction.

B. Resistance vs temperature

Figure 2 shows measurements of the resistance $R_{1\text{-}3}$ [from (1) to (3)] and of the resistance $R_{1\text{-}2}$ [from (1) to (2)] vs temperature T. For $R_{1\text{-}3}$ (across the SLCO/Au/Nb junction), two resistive transitions are visible, which we attribute to the transitions of SLCO ($T_{c,\mathrm{SLCO}} = 15.5$ K) and Nb ($T_{c,\mathrm{Nb}} = 8.7$ K) with transition widths $\Delta T_{c,\mathrm{SLCO}} \approx 2$ K and $\Delta T_{c,\mathrm{Nb}} \approx 0.1$ K, respectively. From Rutherford backscattering spectroscopy we determined a doping of $x \sim 0.15$, which is slightly above the doping of our target.[25] Hence, our films are overdoped, which explains the reduced T_c as compared to optimally doped SLCO with $x \sim 0.10$.[4,12] The residual resistance below $T_{c,\mathrm{Nb}}$ has to be assigned to the SLCO/Au/Nb junction (cf. Sec. III A), which will be discussed in Sec. III C.

The $R_{1\text{-}2}(T)$ curve for the bottom SLCO layer yields a $T_{c,\mathrm{SLCO}}$ which coincides with the SLCO transition measured across the junction, as expected. The inset of Fig. 2 shows $R(T)$ of the unpatterned SLCO/Au/Nb trilayer from the same chip measured prior to junction pattering in a van der Pauw geometry. The resistive transition occurs at 15.5 K, which demonstrates that $T_{c,\mathrm{SLCO}}$ is not affected by the junction patterning process.

For the resistance measurement on the unpatterned trilayer, we expect the normal-state resistance to be dominated by the Au/Nb layer with much lower resistivity as compared to the SLCO layer. Neglecting the contribution from the thin Au layer gives a lower bound for the normal-state resistivity of the Nb film in the trilayer of $\rho_{n,\mathrm{Nb}} \approx 8\ \mu\Omega$ cm. This value is slightly larger than typical $\rho_{n,\mathrm{Nb}}$ values for our Nb thin films; however, this is consistent with the relatively small residual resistance ratio of 2 as determined from the inset shown in Fig. 2.

From the Au/Nb normal-state resistivity as determined above, we can estimate the normal-resistance contribution $R_{n,\mathrm{Au/Nb}}$ of the Au/Nb finger (75 μm long and 5 μm wide) connecting the SLCO/Au/Nb junction with pad 3 (see Fig. 1). This yields $R_{n,\mathrm{Au/Nb}} = 15\ \Omega$, which is in very good agreement with the residual resistance $R_{1\text{-}3}$ measured across the patterned junction in the range $T_{c,\mathrm{Nb}} < T < T_{c,\mathrm{SLCO}}$ (see Fig. 2).

Finally, comparing the values $R_{n,1\text{-}3} = 79\ \Omega$ and $R_{n,1\text{-}2} = 93\ \Omega$ of the normal resistance R_n slightly above $T_{c,\mathrm{SLCO}}$, we find $R_{n,\mathrm{SLCO}} = 58\ \Omega$ for the normal resistance of the bottom SLCO film between pads 1 and 2 and normal-resistance values for the three pads $R_{n,i} = 17.5\ \Omega$ ($i = 1,2,3$), if we assume that they are identical and if we take into account that $R_{n,\mathrm{SLCO}}/2$ will contribute in series with $R_{n,\mathrm{Au/Nb}}$ to $R_{n,1\text{-}3}$. From $R_{n,\mathrm{SLCO}}$ we calculate a normal-state resistivity of the SLCO film $\rho_{n,\mathrm{SLCO}} = 0.12$ mΩ cm, which is within the range of typical values 0.1 to 0.2 mΩ cm for our SLCO films; i.e., the patterning process seems not to severely affect $\rho_{n,\mathrm{SLCO}}$.

C. Current-voltage characteristics

Figure 3(a) shows (current-biased) $I(V)$ characteristics of the SLCO/Au/Nb junction, in the temperature range $4.2 \leqslant T \leqslant 8.9$ K. Two main transitions are visible, the first to $R_{1\text{-}3} = 15\ \Omega$ and the second to $R_{1\text{-}3} = 44\ \Omega$. According to the above discussion of the $R(T)$ curves in Fig. 2, the first transition can be identified as the switching of the Au/Nb finger to the normal state and the second transition to the switching of the SLCO film between pads 1 and 3 to the normal state (with resistance $R_{n,\mathrm{SLCO}}/2 = 29\ \Omega$), which is also consistent with the observation that the second transition persists to temperatures above 8.7 K, i.e., it has to be attributed to SLCO.

In Fig. 3(b), the low-voltage behavior of the $I(V)$ curves is displayed. Two main features are obvious: (i) Cooper pair tunneling is not observed, and (ii) the $I(V)$ curves are nonlinear, possibly due to the presence of an insulating tunneling barrier. This explains the residual resistance below 8.7 K as observed in the $R_{1\text{-}3}(T)$ curve shown in Fig. 2. Both points will be discussed in the following.

1. Absence of Cooper pair tunneling

If the barrier between superconducting Nb and SLCO was (electrically) too thick, no Cooper pair tunneling could be observed. However, a too thick Au interlayer between Nb and SLCO can be ruled out because of the previously described proximity effect. Instead, a plausible explanation might be based on the formation of an oxygen gradient along the c axis of the SLCO film. As described in Sec. II, a reduction step right after SLCO film growth is necessary to obtain superconducting properties. This reduction step possibly generates a gradient, with decreasing oxygen concentration toward the SLCO surface. As shown elsewhere,[25] an oxygen-deficient phase has normal conducting or even insulating electric properties. Such an insulating SLCO surface could act as a tunneling barrier.

2. Nonlinear tunneling curves

By numerical differentiation, the low-voltage regime of the $I(V)$ curves was transformed into differential conductance $dI/dV(V)$ curves, which are shown in Fig. 3(c). A superconducting gap $\Delta \approx 1.4$ meV is visible, which can be assigned to Nb. The presence of the Nb gap is a clear indication for *quasiparticle* tunneling from the superconducting Au/Nb electrode through a tunneling barrier, which is formed near

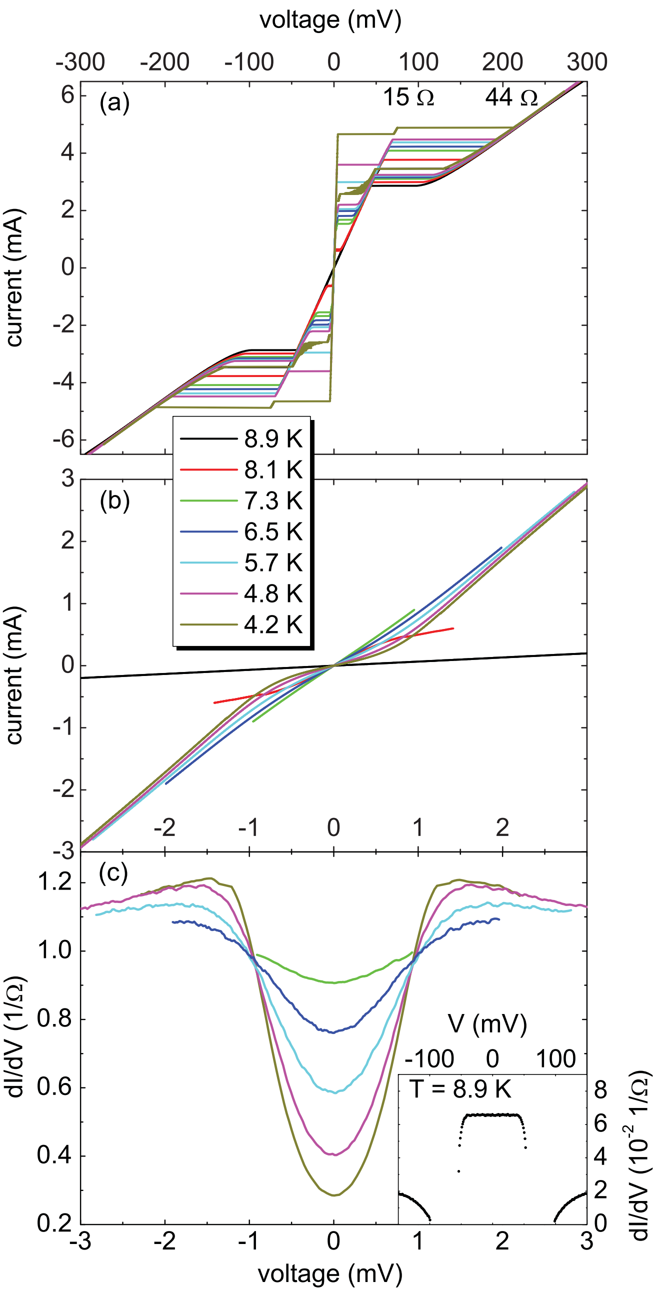

FIG. 3. (Color online) Transport characteristics of a planar SLCO/Au/Nb junction for different temperatures: (a) $I(V)$ curves over large voltage range $|V| \leqslant 300$ mV and (b) zoom-in of low-voltage regime $|V| \leqslant 3$ mV. (c) Differential conductance curves $dI/dV(V)$. Inset shows $dI/dV(V)$ at $T = 8.9$ K on a larger voltage scale.

the SLCO/Au interface, into *normal-conducting* SLCO. We did not find any indication for the presence of an SLCO gap in the $dI/dV(V)$ curves for $T < T_{c,\mathrm{Nb}}$. Furthermore, the inset of Fig. 3(c) shows the $dI/dV(V)$ curve at $T = 8.9\ \mathrm{K} > T_{c,\mathrm{Nb}}$ with a constant conductance and no gaplike feature up to $|V| = 53$ mV. Thus, we have to conclude that there is no tunneling from superconducting SLCO across the barrier. Our data suggest a “stacking” of superconducting SLCO/normal-conducting SLCO/insulating SLCO (tunneling barrier)/superconducting Au/Nb along the sample normal.

IV. X-RAY PHOTOELECTRON SPECTROSCOPY

To examine the chemical state of the SLCO surface, XPS and XAES were performed on the two SLCO thin-film reference samples (SLCO-1 and SLCO-2), which were transferred to the XPS/XAES setup immediately after growth. For data taken after annealing in the XPS/XAES setup we refer to those samples as SLCO-1a and SLCO-2a. The adventitious carbon 1*s* line was used to calibrate the binding-energy scale, assuming a binding energy of 284.6 eV for hydrocarbons. For all XPS data shown below, the peak centers, Gaussian widths, and intensity ratios were determined by numerical fits.[26] For better clarity we do not show the fitting curves in the graphs below. Instead, all fitting results are summarized in Table I.

A. XPS of the infinite-layer phase

Figure 4 shows XP spectra of the O 1*s* (a), the Sr 3*d* (b), and the Cu 2*p* (c) orbitals, for both normal (0°) and grazing (60°)

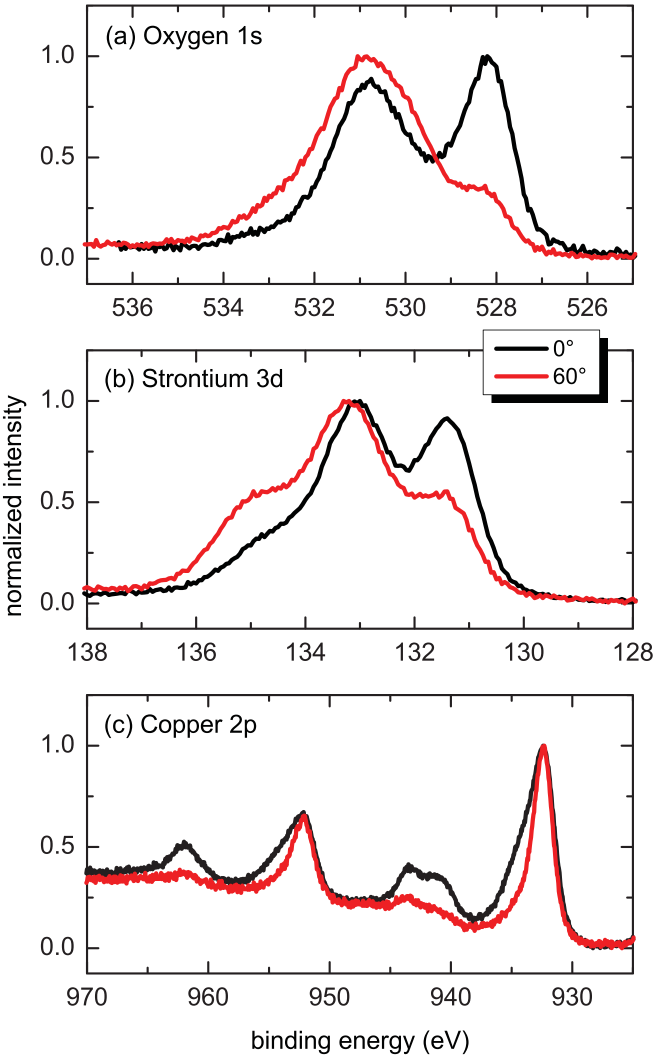

FIG. 4. (Color online) XPS data from SLCO-1 (with IL crystal structure) showing relevant photoemission signals for O 1*s* (a), Sr 3*d* (b), and Cu 2*p* (c) lines at normal incidence 0° and tilt angle 60°, corresponding to information depths of 6 and 3 nm, respectively.

TABLE I. Core-level binding energies (eV) as determined by numerical fitting of the XPS data. The two components (see text) are labeled as 1 and 2, respectively. The Gaussian peak width is denoted in parentheses. The intensity ratio I_1/I_2 is determined by the ratio of the areas beneath the according peaks. For Sr, ΔE denotes the splitting of the doublet ($j = 3/2$ and $5/2$). The superconducting IL bulk component is marked with an asterisk ($*$) and the insulating IL-r bulk component with a dagger (†) (see text). All unmarked components are surface components.

		Cu $2p_{3/2}$			Sr $3d_{5/2}$					O $1s$		
Sample		1	2	I_1/I_2	1	ΔE	2	ΔE	I_1/I_2	1	2	I_1/I_2
SLCO-1	(0°)	932.3(1.6)	934.3(1.5)*	3.5	131.3(1.0)*	1.8	132.7(1.8)	1.7	1.3	528.2(1.1)*	530.7(1.4)	0.6
	(60°)	932.4(1.3)	934.1(1.7)*	8.6	131.4(1.2)*	2.0	133.0(1.4)	1.9	0.5	528.2(0.8)*	530.7(2.8)	0.1
SLCO-2a	(0°)	932.4(1.6)†	933.8(1.5)†	0.8	131.8(1.0)†	1.8	132.8(1.4)	1.8	0.5	528.6(1.0)†		
	(60°)	932.4(1.6)†	934.0(2.0)†	1.4	131.9(1.1)†	1.9	133.0(1.4)	1.8	0.3	528.9(1.5)†	530.5(0.8)	1.3

incidence. The data were collected on the superconducting thin film SLCO-1, which had a single-phase IL crystal structure even after annealing in the XPS/XAES setup, as confirmed by subsequent XRD measurements (see Sec. VI).

1. Oxygen 1s

In Fig. 4(a) two components can be identified in the spectrum. By tilting the sample to 60°, the high-energy peak increased whereas the low-energy one decreased. Thus, the first one is identified as a surface component and the second one as a bulk component.

Vasquez *et al.*[27] showed that the peak at rather low binding energy of 528.2 eV belongs to oxygen in the CuO_2 planes of common electron-doped cuprate superconductors, where copper has a valence of +2. The surface component at 530.7 eV is a mixture of adsorbed oxygen-containing species, mostly water, and compounds like $Sr(OH)_2$ and $SrCO_3$, which may have formed when the sample was in contact with ambient air. Also, surface species of the CuO_2 planes (which are not charge neutral due to the reduced symmetry in the uppermost layer) could contribute to the high-energy peak. We found that this peak drastically decreased upon heating the sample to around (300–350) °C (not shown here), hinting at water contamination because all other compounds are not volatile under the prevailing conditions. However, the high-energy peak did not disappear completely after annealing, supporting the fact that other surface compounds are present.

2. Strontium 3d

Due to spin-orbit coupling, the strontium $3d$ orbital is split into a doublet with $j = 3/2$ and $5/2$. The XPS data shown in Fig. 4(b) reveal a superposition of two doublets. The two peaks within each doublet show a separation of (1.8 ± 0.1) eV and an intensity ratio of 3:2, as expected. For the high- and the low-binding-energy doublets, the $j = 5/2$ line is located at 132.7 and 131.3 eV, respectively. Under grazing incidence, the high-binding-energy doublet gains intensity at the expense of the low-binding-energy doublet. Thus, the first one is identified as a surface component and the second one as a bulk component.

According to Vasquez *et al.*,[27] the bulk doublet originates from the superconducting SLCO phase and the surface doublet from a carbonate ($SrCO_3$). Nevertheless, a hydroxide such as $Sr(OH)_2$ and an oxide such as SrO are also candidates for this surface component. In other studies[28–31] the Sr $3d_{5/2}$ peak for the hole-doped cuprate superconductor $Bi_2Sr_2CaCu_2O_8$ was found at a binding energy of (132.3 ± 0.5) eV, which is close to our result. Compared to the binding energy of elemental Sr at 134.2 eV or of bulk SrO at 135.1 eV,[32] the binding energy found in cuprate superconductors is quite low. This shift toward lower binding energy, as compared to the corresponding metal or simple oxide, is a common feature of various elements in cuprate superconductors.[29] It is the environment and the electronic correlation in these complex materials that lead to this shift.

Upon annealing the sample at (300–350) °C, the half-width of the surface peak increased, but no substantial change in the strontium spectra was observed (not shown here). As mentioned above, Sr-containing contaminations are not volatile under these conditions. The broadening is usually attributed to effects such as charging or nonstoichiometry.

3. Copper 2p

From the Cu $2p$ core-level spectra, the oxidation state of copper can be derived, as found by XPS studies on Cu, Cu_2O, and CuO samples[19,20] as well as on complex high-temperature superconductors like Bi-Sr-Ca-Cu-O (Refs. 28,33) and Y-Ba-Cu-O.[34] In fact, the main lines are known to stem from the screened Cu $2p^5 3d^{10}\underline{L}$ final state of Cu^{2+}, where $\underline{L}$ stands for a hole on the ligand oxygen, and from the screened Cu $2p^5 3d^{10}$ final state of Cu^{1+}, whereas the satellites are known to stem from the unscreened Cu $2p^5 3d^9$ final state of Cu^{2+}. In the latter case, the d shell is not full and the satellite line shape is governed by multiplet splitting, resulting in a broad peak structure.[34,35] The absence of the satellite is thus a fast and reliable sign that there are no Cu^{2+} ions in the compound. Note that the center position of the Cu $2p^{3/2}$ main line is only weakly dependent on the oxidation state of copper: As Tobin *et al.*[36] have shown, the $2p_{3/2}$ peaks of Cu, Cu_2O, and CuO are centered at 932.6, 932.4, and 933.6 eV, corresponding to Cu^0, Cu^{1+}, and Cu^{2+} valences, respectively. This allows us to distinguish Cu^{2+} from a reduced species, Cu^{1+} or Cu^0, but not to distinguish Cu^{1+} from Cu^0. For that purpose, we refer to the Auger-emission studies presented in Sec. V.

The Cu $2p$ spectrum of our sample shown in Fig. 4(c) has a doublet with main lines at 932.3 eV (Cu $2p_{3/2}$) and 952.2 eV (Cu $2p_{1/2}$). A closer look reveals a shoulder on the high-binding-energy side of these lines, indicating the presence of a second copper species. The lines of this species are situated at 934.3 and 954.2 eV. Moreover, satellites at

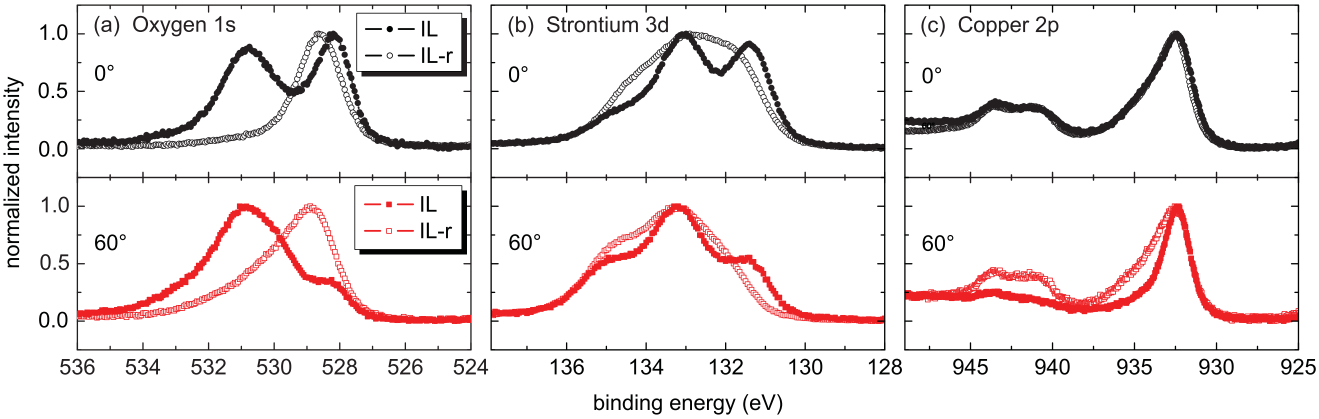

FIG. 5. (Color online) Comparison of XP spectra of the superconducting IL (full symbols) and the insulating IL-r sample (open symbols). Upper graphs show normal (0°) and lower graphs grazing incidence (60°) for O 1s (a), Sr 3d (b), and Cu 2p (c). The clear differences between the spectra allow us to exactly identify the superconducting phase as well as surface contaminations.

around 942 and 962 eV are visible. Tilting our sample, i.e., decreasing the information depth, leads to the disappearance of the satellites and the high-energy doublet. Accordingly, the surface component is identified as a (strongly) reduced copper species with Cu^{1+} or Cu^{0} valence, whereas the bulk component is clearly identified as the oxidized phase with Cu^{2+} valence, which is expected for CuO_2 planes in common cuprate superconductors. Note, that electric transport measurements on our SLCO thin films[25] showed that excessive vacuum annealing of a previously superconducting film leads to loss of superconductivity. This allows us to interpret the oxidized bulk phase as the superconducting phase and the reduced surface phase as a normal-conducting phase. This is an important result because it goes hand in hand with the results of the planar tunneling measurements described in Sec. III C.

In addition to SLCO-1 and SLCO-2, we investigated another sample (not shown here), called SLCO-3, which was not vacuum annealed right after deposition. Instead, it was immediately cooled down *in situ* (while the pressure was reduced to 10^{-5} Pa) to room temperature and was hence less reduced as compared to SLCO-1. This was confirmed by means of XPS: Under normal incidence, both the satellites and the main lines characteristic for Cu^{2+} were more strongly developed in SLCO-3 as compared to SLCO-1. Furthermore, after annealing SLCO-1 at (300–350) °C in the XPS chamber, the Cu^{2+} species decreased slightly (not shown here). Thus, comparing the Cu 2p XP spectra of SLCO-1, SLCO-1a, and SLCO-3, we find that the Cu^{2+} lines decreased with increasing annealing time, i.e., we clearly see the effect of vacuum annealing on the Cu valence.

B. XPS of the infinite-layer-related phase

Sample SLCO-2a was vacuum annealed in the XPS/XAES setup at 550 °C for 5 min. During this procedure, a substantial secondary phase emerged, as shown in Sec. VI by means of XRD. This oxygen-deficient phase is called the long-c-axis phase or infinite-layer-related phase. It is characterized by ordered oxygen vacancies.[15,18] As shown elsewhere,[25] the IL-r phase is electrically insulating and not superconducting.

For simplicity, in the following the sample SLCO-1 is referred to as "IL" (because of its single-phase IL crystal structure) and the annealed sample SLCO-2a is referred to as "IL-r" (because of its dominant IL-r crystal structure). The XP spectra of the IL-r phase differ strongly from those of the IL phase. For comparison, both spectra are shown in Fig. 5. Additionally, the relevant XPS data of the IL-r phase are summarized in Table I, labeled as SLCO-2a, allowing a direct comparison with the XPS data of the IL phase, labeled as SLCO-1.

1. Oxygen 1s

The IL-r spectra in Fig. 5(a) exhibit two components, a weak surface component at high binding energy (530.5 eV) and a strong bulk component at low binding energy (528.8 ± 0.2 eV). The bulk peak of the IL phase at 528.2 eV is absent in the IL-r spectra. Note that superconductivity is also absent in the IL-r phase. Thus, we can definitely assign the peak at 528.2 eV to the superconducting phase, confirming the discussion of Sec. IV A. The IL-r surface component at 530.5 eV was also present on the surface of the IL sample. As discussed before, this component can possibly be identified as SrCO_3 or $\mathrm{Sr(OH)}_2$. However, as the spectral weight of this surface component decreased strongly upon vacuum annealing at 550 °C, some of the adsorbates must have been evaporated. At these elevated temperatures, water may no longer be found and also $\mathrm{Sr(OH)}_2$ should have desorbed.

2. Strontium 3d

As for oxygen, the Sr spectra of the IL-r phase differ strongly from those of the IL phase, as shown in Fig. 5(b). The IL-r spectra exhibit two doublets, i.e., two components, with the high-energy one at $E_{5/2} = (132.9 \pm 0.1)$ eV on the surface and the low-energy one at $E_{5/2} = (131.9 \pm 0.1)$ eV in the bulk. The two peaks (for $j = 5/2$ and $j = 3/2$) within each doublet are separated by (1.8 ± 0.1) eV. The bulk doublet of superconducting IL at $E_{5/2} = (131.4 \pm 0.1)$ eV is absent in the spectra of the nonsuperconducting IL-r phase. Thus, we can pinpoint this doublet to the superconducting phase, confirming the discussion of Sec. IV A. Instead, the bulk component of the IL-r phase shows a positive chemical shift of +0.5 eV compared to SLCO. This result is consistent with the findings of Nagoshi *et al.*[37] They showed that the core-level energies of

$Bi_2Sr_2CaCu_2O_8$, $YBa_2Cu_3O_7$, and related cuprates are lower in the superconducting and higher in the normal-conducting phase. They attribute this to a different Madelung potential due to changes in bond length with varying charge carrier concentrations in the copper oxide planes. Moreover, the absolute binding energies are comparable to our results, both for superconducting and for normal-conducting samples. Finally, the IL-r surface doublet was also present in the IL surface phase. As discussed before, this component can possibly be ascribed to $SrCO_3$ or $Sr(OH)_2$, i.e., to surface adsorbates.

3. *Copper 2p*

Figure 5(c) shows that the 0° *and* 60° spectra of the IL-r phase are very similar to the 0° spectrum of the IL phase. As discussed in Sec. IV A, the 0° spectrum of the IL phase shows two components, an oxidized bulk component with Cu^{2+} valence and a reduced surface component with Cu^{1+} or Cu^0 valence. As the IL-r spectrum does not show a pronounced dependence on the information depth, we can conclude that Cu of different valences is distributed throughout the *entire* IL-r sample and none of them is restricted to the surface, in contrast to the IL sample.

To identify the valence of the reduced species, either Cu^{1+} or Cu^0, we performed x-ray Auger-electron spectroscopy. The results for both samples, IL and IL-r, are presented in Sec. V.

V. X-RAY AUGER-ELECTRON SPECTROSCOPY

While the satellite in the Cu $2p$ XP spectrum is a clear indication for Cu^{2+}, it is much harder to distinguish between Cu^0 and Cu^{1+}, because the main lines are overlapping. For this purpose, we examined the Cu $L_3M_{45}M_{45}$ Auger signal, which changes not only its position depending on the valence, but also its shape. The initial states of the Cu $L_3M_{45}M_{45}$ Auger process are the final states of the Cu $2p$ XP process, i.e., $2p^53d^{10}\underline{L}$ and $2p^53d^9$ for divalent copper and $2p^53d^{10}$ for monovalent copper. The corresponding Auger final states are $3d^8\underline{L}$ and $3d^7$ for divalent copper and $3d^8$ for monovalent copper.[19] In CuO, Cu_2O, and Cu samples, the Auger main lines were detected at kinetic energies of (918.0 ± 0.2), (916.7 ± 0.2), and (918.6 ± 0.2) eV, corresponding to divalent, monovalent, and elemental Cu, respectively.[21,36,38,39] However, in superconducting cuprates like Bi-Sr-Ca-Cu-O (Refs. 28 and 29) and Y-Ba-Cu-O,[34] the Cu $L_3M_{45}M_{45}$ lines are typically shifted by +0.5 eV due to the more complex chemical environment.

In Fig. 6 we present XAES data of the IL phase, the IL-r phase, and a Cu foil.[40] The Cu foil, serving as a reference for Cu^0, had a purity of 99.9 % and was cleaned *in situ* by sputtering prior to measurement. For all spectra, the intensities are normalized to zero at a kinetic energy of 930 eV and to unity at 910 eV. For better clarity, the different curves are shifted equidistantly along the vertical axis (normalized intensity) by 1. The dashed lines at 917.2, 918.5, and 919.1 eV indicate the values for Cu^{1+}, Cu^{2+}, and Cu^0 according to the literature, shifted by the above-mentioned +0.5 eV to account for the effect of the chemical environment. For the same reason, the Cu^0 spectrum was shifted by +0.5 eV as well. The characteristic structure of the Cu^0 spectrum from the Cu foil with its sharp main line and its multiplet features[41] allows for an unambiguous identification of elemental Cu.

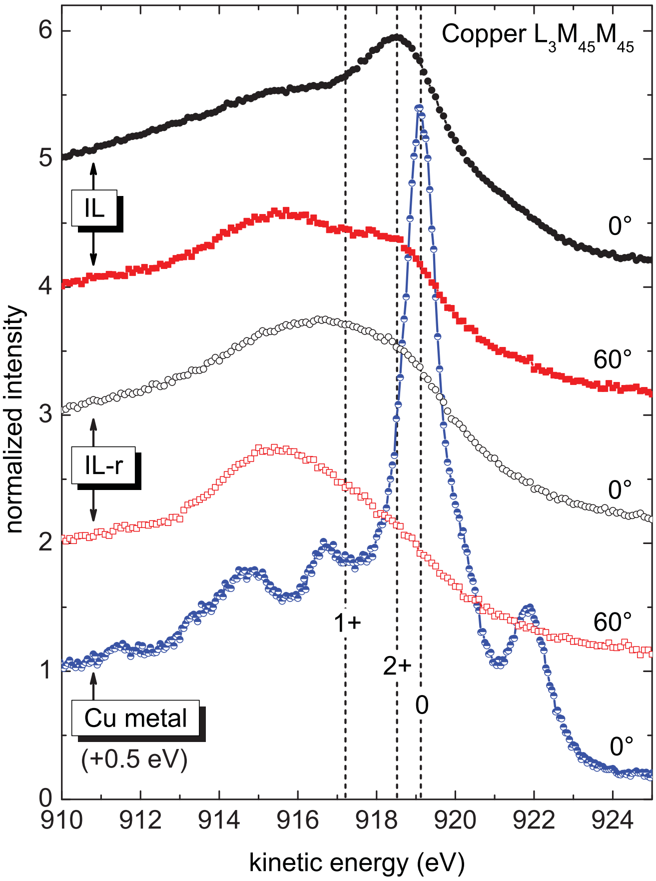

FIG. 6. (Color online) X-ray excited Cu $L_3M_{45}M_{45}$ Auger spectra of superconducting IL, insulating IL-r, and Cu reference sample, for normal (0°) and grazing incidence (60°). Curves are shifted equidistantly along the vertical axis by 1. The dashed lines indicate the peak positions of Cu^0, Cu^{1+}, and Cu^{2+} as expected for cuprate superconductors according to the literature (see text).

In the IL and IL-r spectra shown in Fig. 6, two main peaks are visible, one centered at ~915 eV and the other at 918.5 eV. The two peaks are clearly separate in the IL phase but broadened and overlapping in the IL-r phase. We want to point out that a satellite, typically centered at 912–915 eV, is a common Auger feature of copper, copper oxides, copper dihalides, and superconducting cuprates. As the discussion of the satellite goes beyond the scope of this work, we refer to the work of Ramaker[42] and the literature cited therein. In the following, we will therefore focus on the main line.

A. XAES of the infinite-layer phase

As in our XP spectra, we can identify an XAES peak in Fig. 6 related to the superconducting phase, now at 918.5 eV, which is most prominent in the IL sample at normal emission. This peak has also been observed at the same energy in hole-doped cuprate superconductors like Y-Ba-Cu-O (Ref. 34) and Bi-Sr-Ca-Cu-O.[28,29] There, the Cu valence relating to this peak was determined as +2, in accordance with our XPS studies presented in Sec. IV A. We can further rule out the possibility that this peak stems from elemental Cu because it is not possible to generate elemental Cu by an annealing step similar to ours[20,21] and because elemental Cu is highly susceptible to reoxidation in ambient air, even at room temperature. Furthermore, in contrast to the sharp main line of Cu^0, the main line of our IL sample is much broader. This broadening is generally observed in various copper oxides, such as Cu_2O, CuO, Bi-Sr-Ca-Cu-O, or Y-Ba-Cu-O, and it is attributed to Cu d–O p hybridization.[35]

Together with our XPS results (cf. Sec. IV A), we can now identify the valence of the reduced surface species as +1 and rule out elemental Cu due to its absence in the Auger spectra. As described above, we expect a line relating to Cu^{1+} in our Auger spectra at a kinetic energy of 917.2 eV. Indeed, a shift of the spectral weight toward lower kinetic energy was observed upon tilting the sample, hinting at Cu^{1+}. Yet a clear peak was not observed.

B. XAES of the infinite-layer-related phase

The XPS analysis on the IL-r phase did not reveal a remarkable variation of the Cu valence with information depth [cf. Fig. 5 (c)]. Again, XAES gives some more insight into this system, showing that there is some difference between bulk and surface (cf. Fig. 6). The broad XAES bulk spectrum with its maximum at 916.6 eV can only be explained by a superposition of peaks stemming from Cu^{2+} and Cu^{1+} as well as the satellite, in full agreement with our XPS results. Upon tilting, the spectral weight shifted toward lower kinetic energy, pointing to a dominant Cu^{1+} species on the surface. However, a weak signal relating to Cu^{2+} is still visible in the surface spectrum, again in agreement with our XPS results.

We can finally calculate the Auger parameter,[43] which is defined as the sum of the core-level binding energy (e.g., Cu $2p_{3/2}$) and the kinetic energy of the appropriate Auger electron (e.g., Cu $L_3M_{45}M_{45}$). For Cu^{2+} we find $934.1 + 918.5 = 1852.6$ eV and for Cu^{1+} $932.4 + 916.6 = 1849.0$ eV. Note that those values are even more strongly separated from each other than those reported for Bi-Sr-Ca-Cu-O (1851.8 and 1848.9 eV),[28] or for CuO and Cu_2O (1851.7 and 1848.9 eV).[36]

To conclude with Secs. IV and V, we detected divalent Cu in the bulk of the IL and mono- and divalent Cu in the bulk of the IL-r samples. Upon increasing the surface sensitivity, we found dominantly monovalent Cu on top of all samples.

VI. X-RAY DIFFRACTION

A. XRD of the infinite-layer phase

Figure 7 shows XRD data of the two films SLCO-1a and SLCO-2a that were previously examined by XPS and XAES (see Secs. IV and V). Both samples are c-axis oriented, as found by ϕ scans (not shown here). For SLCO-1a, which was vacuum annealed at 350 °C, no secondary phase could be identified, even in high-resolution Θ-2Θ scans, i.e., the sample is single phase with IL crystal structure and a c-axis parameter of 3.402 Å. Laue oscillations are visible, indicating high crystallographic quality along the film normal. The film thickness calculated from these oscillations is 23 ± 1 nm, corresponding to 68 ± 3 unit cells (uc). Reciprocal space mapping of the SLCO (303) peak showed a very sharp peak without any extensions along the (100) direction (not shown here), i.e., the film is coherently strained. The in-plane lattice parameter was determined as 3.987 ± 0.002 Å which is close to the lattice parameter of the cubic KTO template, 3.9883 Å.

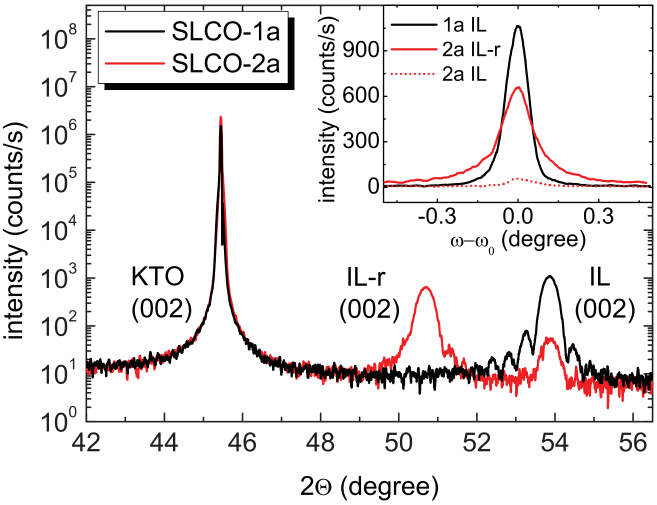

FIG. 7. (Color online) XRD data of (single-phase) IL thin-film SLCO-1a and of the strongly vacuum-annealed thin-film SLCO-2a with dominant IL-r phase. Main graph shows Θ-2Θ scans. Inset shows rocking curves around the (002) peaks.

RHEED oscillations during film growth indicated a film thickness of 76 ± 3 uc, corresponding to 26 ± 1 nm, in contrast to the thickness determined by Laue oscillations. The thickness difference of a few nanometers can be attributed either to a defect-rich interface region close to the substrate or to a disordered film surface. Indeed, by means of XPS and XAES (see Secs. IV and V), a reduced SLCO surface layer with dominantly monovalent Cu was identified. We therefore favor the latter interpretation. Yet the absence of any signs of an IL-r phase in the XRD data of SLCO-1a implies that the reduced surface is *not* the IL-r phase. One possible explanation would be that the reduced surface still has an IL crystal structure but with (unordered) oxygen vacancies in the CuO_2 planes.

B. XRD of the infinite-layer-related phase

SLCO-2a, which was vacuum annealed at 550 °C, has an IL-r phase as major component and the IL phase as minor component. The c-axis parameters were determined as 3.598 Å for the major and 3.400 Å for the minor component. Again, Laue oscillations indicate high crystallographic quality along the film normal. With the aid of these oscillations, the film thickness was determined as 23 ± 2 nm for IL-r and 22 ± 2 nm for the infinite layer, i.e., the two phases coexist side by side and not on top of each other.

These results imply that the formation of the IL-r phase is not a process that develops along the film normal (from the surface to the bottom or vice versa) but it develops laterally on distinct nuclei. As shown elsewhere,[25] the coexistence of those two phases can even be imaged with an optical microscope due to their different optical reflection. We observed islandlike areas, which supports our interpretation of the XRD data described here. Moreover, the rocking curve of the IL-r (002) peak (for SLCO-2a) shows an increased full width at half maximum $\Delta\omega = 0.14^\circ$ compared to the single-phase IL (002) peak (for SLCO-1a) with $\Delta\omega = 0.10^\circ$. We interpret this as a fingerprint of lattice distortions due to the coexistence of the two phases.

VII. CONCLUSIONS

We fabricated *in situ*–grown planar thin-film SLCO/Au/Nb junctions and investigated their electric transport properties. Our in-plane transport data show that below the Nb transition temperature, both electrodes are in the superconducting state. Regarding out-of-plane electric transport across the junctions, the absence of Cooper pair tunneling and the presence of quasiparticle tunneling from superconducting Nb (identified by a clear gap feature) to normal-conducting SLCO clearly indicates the presence of an insulating SLCO barrier layer on top of a normal conducting SLCO layer at the interface between the superconducting bottom SLCO electrode and the Au interlayer. Such an insulating/normal-conducting SLCO surface layer is likely to be formed during vacuum annealing of the infinite layer cuprate superconductor SLCO after film growth.

In order to check the interpretation of our electric transport data, we examined the electronic structure and valence states of the SLCO surface layer. This was done by performing XPS and XAES measurements on two SLCO thin films, which were fabricated under nominally identical conditions as for the bottom SLCO electrode in the SLCO/Au/Nb junctions. After high-temperature vacuum annealing in the XPS/XAES setup, one of the two SLCO films was reduced, which transformed this film predominantly into the infinite-layer-related phase, while the other film was examined as representative for the IL phase. Upon tilting the IL sample (reducing the XPS/XAES information depth from ~6 to ~3 nm), we identified a reduced surface (with Cu valence +1 or 0) and oxidized bulk (with Cu valence +2) component via XPS measurements. In order to determine the Cu valences at the surface, XAES measurements were performed, which identified Cu^{1+} on the surface of both the IL and IL-r samples. The comparison of XP spectra of superconducting IL and nonsuperconducting IL-r samples allows us to relate the bulk signals for Sr, O, and Cu in the IL sample to the superconducting IL phase. Moreover, this comparison also allows us to identify the signatures of the IL-r component in the XP/XAE spectra and shows that the unit cell of the IL-r compound contains mixed Cu valences (+1 and +2). X-ray diffraction data indicate a disordered surface layer of ~3 nm thickness, which is consistent with both the XPS/XAES data and the out-of-plane transport data.

We can consistently interpret all our data, if we assume that the SLCO surface layer with Cu valence +1 is insulating. A likely scenario for its formation is the formation of a gradient of disordered oxygen vacancies along the SLCO film normal within the uppermost few nanometers. This could be due to the annealing step right after film deposition, and hence should occur for the SLCO films as well as for the SLCO films within the SLCO/Au/Nb trilayer structures. On the one hand, such a gradient of oxygen vacancies can explain the XPS/XAES data (i.e., change in Cu valence states from +2 in the bulk to +1 on the surface). On the other hand, such a gradient can be assumed to change the SLCO films from superconducting to normal conducting and finally insulating, along the surface normal, close to the SLCO film surface or SLCO/Au interface. This is supported by our out-of-plane transport data. Hence, our electric transport data for the SLCO/Au/Nb junctions are fully consistent with the XPS/XAES and XRD data on our SLCO thin films.

ACKNOWLEDGMENTS

J.T. gratefully acknowledges support by the Evangelisches Studienwerk e. V. Villigst. V.L. acknowledges partial financial support by the Romanian Ministry of Education and Research (Human Resources Reintegration Project No. 1476/2006) and by CNCSIS-UEFISCSU (Project No. PNII-IDEI ID_743/2007). This work was funded by the Deutsche Forschungsgemeinschaft (Project No. KL 930/11).

---

[*] koelle@uni-tuebingen.de

[1] Y. Tokura, H. Takagi, and S. Uchida, Nature (London) **337**, 345 (1989).

[2] H. Takagi, S. Uchida, and Y. Tokura, Phys. Rev. Lett. **62**, 1197 (1989).

[3] M. G. Smith, A. Manthiram, J. Zhou, J. B. Goodenough, and J. T. Markert, Nature (London) **351**, 549 (1991).

[4] G. Er, S. Kikkawa, F. Kanamaru, Y. Miyamoto, S. Tanaka, M. Sera, M. Sato, Z. Hiroi, M. Takano, and Y. Bando, Physica C **196**, 271 (1992).

[5] H. Shaked, Y. Shimakawa, B. A. Hunter, R. L. Hitterman, J. D. Jorgensen, P. D. Han, and D. A. Payne, Phys. Rev. B **51**, 11784 (1995).

[6] T. Siegrist, S. M. Zahurak, D. W. Murphy, and R. S. Roth, Nature (London) **334**, 231 (1988).

[7] G. Er, Y. Miyamoto, F. Kanamaru, and S. Kikkawa, Physica C **181**, 206 (1991).

[8] N. Ikeda, Z. Hiroi, M. Azuma, M. Takano, Y. Bando, and Y. Takeda, Physica C **210**, 367 (1993).

[9] J. D. Jorgensen, P. G. Radaelli, D. G. Hinks, J. L. Wagner, S. Kikkawa, G. Er, and F. Kanamaru, Phys. Rev. B **47**, 14654 (1993).

[10] C. Niu and C. M. Lieber, Appl. Phys. Lett. **61**, 1712 (1992).

[11] H. Adachi, T. Satoh, Y. Ichikawa, K. Setsune, and K. Wasa, Physica C **196**, 14 (1992).

[12] S. Karimoto, K. Ueda, M. Naito, and T. Imai, Appl. Phys. Lett. **79**, 2767 (2001).

[13] M. Naito, H. Sato, and H. Yamamoto, Physica C **293**, 36 (1997).

[14] Z. Z. Li, V. Jovanovic, H. Raffy, and S. Megtert, Physica C **469**, 73 (2009).

[15] V. Leca, D. H. A. Blank, G. Rijnders, S. Bals, and G. van Tendeloo, Appl. Phys. Lett. **89**, 092504 (2006).

[16] V. Leca, G. Visanescu, C. Back, R. Kleiner, and D. Koelle, Appl. Phys. A **93**, 779 (2008).

[17] S. I. Karimoto and M. Naito, Appl. Phys. Lett. **84**, 2136 (2004).

[18] B. Mercey, A. Gupta, M. Hervieu, and B. Raveau, J. Solid State Chem. **116**, 300 (1995).

[19] J. Ghijsen, L. H. Tjeng, J. van Elp, H. Eskes, J. Westerink, G. A. Sawatzky, and M. T. Czyzyk, Phys. Rev. B **38**, 11322 (1988).

[20] S. Poulston, P. M. Parlett, P. Stone, and M. Bowker, Surf. Interface Anal. **24**, 811 (1996).

[21] P. D. Kirsch and J. G. Ekerdt, J. Appl. Phys. **90**, 4256 (2001).

[22] Chemco GmbH, Germany.

[23] Crystal GmbH, Germany.

[24] See Supplemental Material at http://link.aps.org/supplemental/10.1103/PhysRevB.84.064521 for Electric transport across $Sr_{1-x}La_xCuO_2$/Au/Nb planar tunnel junctions and x-ray photoelectron and Auger-electron spectroscopy on $Sr_{1-x}La_xCuO_2$ thin films.

[25] V. Leca *et al.* (unpublished).

[26] Computer code UNIFIT, Spectrum Processing, Analysis and Presentation Software for Photoelectron Spectra, Unifit Scientific Software GmbH, University Leipzig, Germany.

[27] R. P. Vasquez, C. U. Jung, J. Y. Kim, M.-S. Park, H.-J. Kim, and S.-I. Lee, J. Phys.: Condens. Matter **13**, 7977 (2001).

[28] S. Kohiki, K. Hirochi, H. Adachi, K. Setsune, and K. Wasa, Phys. Rev. B **38**, 9201 (1988).

[29] F. U. Hillebrecht, J. Fraxedas, L. Ley, H. J. Trodahl, J. Zaanen, W. Braun, M. Mast, H. Petersen, M. Schaible, L. C. Bourne *et al.*, Phys. Rev. B **39**, 236 (1989).

[30] P. Kulkarni, S. K. Kulkarni, A. S. Nigavekar, S. K. Agarwal, V. P. S. Awana, and A. V. Narlikar, Physica C **166**, 530 (1990).

[31] R. P. Vasquez, J. Electron Spectrosc. Relat. Phenom. **56**, 217 (1991).

[32] H. van Doveren and J. A. T. Verhoeven, J. Electron Spectrosc. Relat. Phenom. **21**, 265 (1980).

[33] P. Alméras, H. Berger, and G. Margaritondo, Solid State Commun. **87**, 425 (1993).

[34] D. van der Marel, J. van Elp, G. A. Sawatzky, and D. Heitmann, Phys. Rev. B **37**, 5136 (1988).

[35] G. van der Laan, C. Westra, C. Haas, and G. A. Sawatzky, Phys. Rev. B **23**, 4369 (1981).

[36] J. P. Tobin, W. Hirschwald, and J. Cunningham, Appl. Surf. Sci. **16**, 441 (1983).

[37] M. Nagoshi, Y. Syono, M. Tachiki, and Y. Fukuda, Phys. Rev. B **51**, 9352 (1995).

[38] S. W. Gaarenstroom and N. Winograd, J. Chem. Phys. **67**, 3500 (1977).

[39] R. J. Bird and P. Swift, J. Electron Spectrosc. Relat. Phenom. **21**, 227 (1980).

[40] Goodfellow GmbH, Germany.

[41] S. P. Kowalczyk, R. A. Pollak, F. R. McFeely, L. Ley, and D. A. Shirley, Phys. Rev. B **8**, 2387 (1973).

[42] D. E. Ramaker, J. Electron Spectrosc. Relat. Phenom. **66**, 269 (1994).

[43] C. D. Wagner, Anal. Chem. **44**, 967 (1972).